High-speed silicon photonic electro-optic Kerr modulation

Jonathan Peltier, Weiwei Zhang, Leopold Virot, Christian Lafforgue, Lucas Deniel, Delphine Marris-Morini, Guy Aubin, Farah Amar, Denh Tran, Xingzhao Yan, et al.

Research Article Vol. 12, No. 1 / January 2024 / Photonics Research 51

PHOTONICS Research

High-speed silicon photonic electro-optic Kerr modulation

Jonathan Peltier,[1,2,4] Weiwei Zhang,[3,5] Leopold Virot,[2] Christian Lafforgue,[1] Lucas Deniel,[1] Delphine Marris-Morini,[1] Guy Aubin,[1] Farah Amar,[1] Denh Tran,[3] Xingzhao Yan,[3] Callum G. Littlejohns,[3] Carlos Alonso-Ramos,[1] Ke Li,[3] David J. Thomson,[3] Graham Reed,[3] and Laurent Vivien[1]

[1]University Paris-Saclay, CNRS, Centre for Nanoscience and Nanotechnology (C2N), Palaiseau 91120, France
[2]University Grenoble Alpes, CEA, LETI, Grenoble 38000, France
[3]Optoelectronics Research Centre, Zepler Institute for Photonics and Nanoelectronics, Faculty of Engineering and Physical Sciences, University of Southampton, Southampton SO17 1BJ, UK
[4]e-mail: jonathan.peltier@c2n.upsaclay.fr
[5]e-mail: Weiwei.Zhang@soton.ac.uk

Received 28 February 2023; revised 28 June 2023; accepted 7 August 2023; posted 8 August 2023 (Doc. ID 488867); published 14 December 2023

Silicon-based electro-optic modulators contribute to easing the integration of high-speed and low-power consumption circuits for classical optical communications and data computations. Beyond the plasma dispersion modulation, an alternative solution in silicon is to exploit the DC Kerr effect, which generates an equivalent linear electro-optical effect enabled by applying a large DC electric field. Although some theoretical and experimental studies have shown its existence in silicon, limited contributions relative to plasma dispersion have been achieved in high-speed modulation so far. This paper presents high-speed optical modulation based on the DC Kerr effect in silicon PIN waveguides. The contributions of both plasma dispersion and Kerr effects have been analyzed in different waveguide configurations, and we demonstrated that the Kerr induced modulation is dominant when a high external DC electric field is applied in PIN waveguides. High-speed optical modulation response is analyzed, and eye diagrams up to 80 Gbit/s in NRZ format are obtained under a d.c. voltage of 30 V. This work paves the way to exploit the Kerr effect to generate high-speed Pockels-like optical modulation.

https://doi.org/10.1364/PRJ.488867

1. INTRODUCTION

Integrated electro-optic (EO) modulators are a key component in systems such as classical and quantum optical communications, photonics-based quantum computing, and sensing. These systems target high-speed and low power consumption optical modulators. Silicon (Si) modulators, which rely primarily on the plasma dispersion effect [1], are intrinsically limited in speed due to their high RC constant [2]. Si modulators relying on the Pockels effect could overcome these limitations to produce a fast and pure phase modulation. Since silicon does not have a natural $\chi^{(2)}$ due to its centrosymmetric structure, such modulation cannot be achieved directly except by straining the crystal lattice [3] leading to a low resulting Pockels coefficient. The integration of high-$\chi^{(2)}$ materials on the Si platform has been widely considered. These include doped polymers, barium titanate (BTO) [4], lead zirconate titanate (PZT) [4], and lithium niobate (LN) [4]. These approaches require the development of hybrid or heterogeneous integration processes that increase the technology complexity. An EO modulation in Si can also be achieved through the DC Kerr effect that electrically induces an effective $\chi^{(2)}$, which can be, hence, exploited to vary the refractive index by applying an electrical modulation superimposed to a static field. The DC Kerr effect has been studied in bulk silica [5], bulk silicon [6,7], silicon interface [8], bulk antiferromagnetic NiO [9], and in integrated platforms including silicon–organic hybrid [10], silicon-rich nitride [11], silicon rich carbide [12], and silicon nitride [13]. It has also been studied in the silicon platform for electric field-induced (EFI) second-harmonic generation (EFISHG) [14], EO modulation (EOM) [15,16], slow light regime [17], and cryogenic experiments [18]. However, the high-speed EOM in Refs. [15–17] using PN junctions led to a plasma dispersion effect that has a higher contribution to the modulation than the DC Kerr effect. While the DC Kerr effect has been well studied in the DC regime, no assessment discriminating the contribution of the DC Kerr effect and

plasma dispersion modulation in the dynamic regime has been reported to our knowledge. This paper presents a comprehensive analysis of the DC Kerr effect induced in a PIN diode inserted in a silicon Mach–Zehnder interferometer (MZI) in both static and dynamic regimes. Data transmission has been analyzed up to 100 Gbit/s in non-return-to-zero (NRZ) format. An experimental method has been developed to assess the relative contribution of plasma dispersion from the Kerr effect in the dynamic regime.

The DC Kerr effect, also known as EFI Pockels effect, originates from the third-order nonlinear susceptibility tensor $\chi^{(3)}$ in presence of a static electric field. The refractive index change induced by the Kerr effect when a static electric field F_{DC} and an RF field $F_{\mathrm{RF}}\cos\Omega t$ are applied to the PIN junction is given by [10]

$$\Delta n(t) = \frac{3\chi^{(3)}}{2n_{\mathrm{si}}}\left(F_{\mathrm{DC}}^2 + \frac{1}{2}F_{\mathrm{RF}}^2 + 2F_{\mathrm{DC}}F_{\mathrm{RF}}\cos\Omega t + \frac{1}{2}F_{\mathrm{RF}}^2\cos 2\Omega t\right), \tag{1}$$

with $\Omega = 2\pi f$, f being the RF frequency, $n_{\mathrm{si}} = 3.48$ being the silicon refractive index, and $\chi^{(3)} = 2.8\times10^{-19}\ \mathrm{m^2\cdot V^{-2}}$ at $\lambda = 1.55\ \mu\mathrm{m}$ for a silicon waveguide with a cross section oriented along the crystallographic axis [110] [19,20]. Equation (1) exhibits three kinds of dependencies. The first one corresponds to the static refractive index growing with the square of the field amplitudes that will be called later the DC Kerr effect concerning F_{DC}. The second one relies on an index modulation at an angular frequency Ω, which has its amplitude growing with the product of the DC and RF field amplitudes. It will be called later the EFI linear EO effect. At last an index modulation at a 2Ω component exhibits an amplitude growing with the square of the RF field amplitude alone. It will be called later the quadratic EO effect.

2. RESULTS AND DISCUSSION

Static and dynamic studies are conducted to distinguish Kerr effects from plasma dispersion on the index variation in three different unbalanced Mach–Zehnder modulators (MZMs). They consist of either PN or PIN junctions named PN, PIN2, PIN3, and their respective intrinsic region widths are $w = 0$, 0.33, and 1.05 μm (Fig. 1). Each junction waveguide has the same cross-sectional design with a 450 nm width, a 220 nm height, and a 100 nm slab thickness, suitable for the propagation of a single TE polarization mode (Appendix G, Fig. 10). The unbalancing of the MZMs is realized by a length difference $\Delta L = 200\ \mu\mathrm{m}$ between the arms leading to a passive phase shift $\Delta\theta = 2\pi/\lambda n_g \Delta L$ with $n_g = 3.6$, the group index of our waveguide. The operating point of the MZM can, thus, be adjusted at the quadrature ($\Delta\theta = \pi/2$) without the need of heaters by only tuning the laser wavelength around 1550 nm.

A. Measurement of the DC Kerr Modulation

The first experiments focus on the comparison between the three junctions in MZMs under a DC bias voltage only. The variation of the effective index of the guided mode (Δn_{DC}) as a function of the reverse DC voltage (V_{DC}) applied to the junction is obtained by measuring the shift of the resonance wavelength $\Delta\lambda_r$,

$$\Delta n_{\mathrm{DC}}(V_{\mathrm{DC}}) = \frac{\lambda_r \Delta\lambda_r(V_{\mathrm{DC}})}{\mathrm{FSR}(\lambda_r)L}, \tag{2}$$

with λ_r being the resonance wavelength, $\mathrm{FSR}(\lambda_r)$ the free spectral range of the MZM, and L the length of the electrodes all along the junctions. See Appendix A. Optical and EO simulations taking into account the DC Kerr and plasma dispersion effects were performed to design the three different PN/PIN waveguides. The measured and simulated variations of the effective index of the three junctions are presented in Fig. 1.

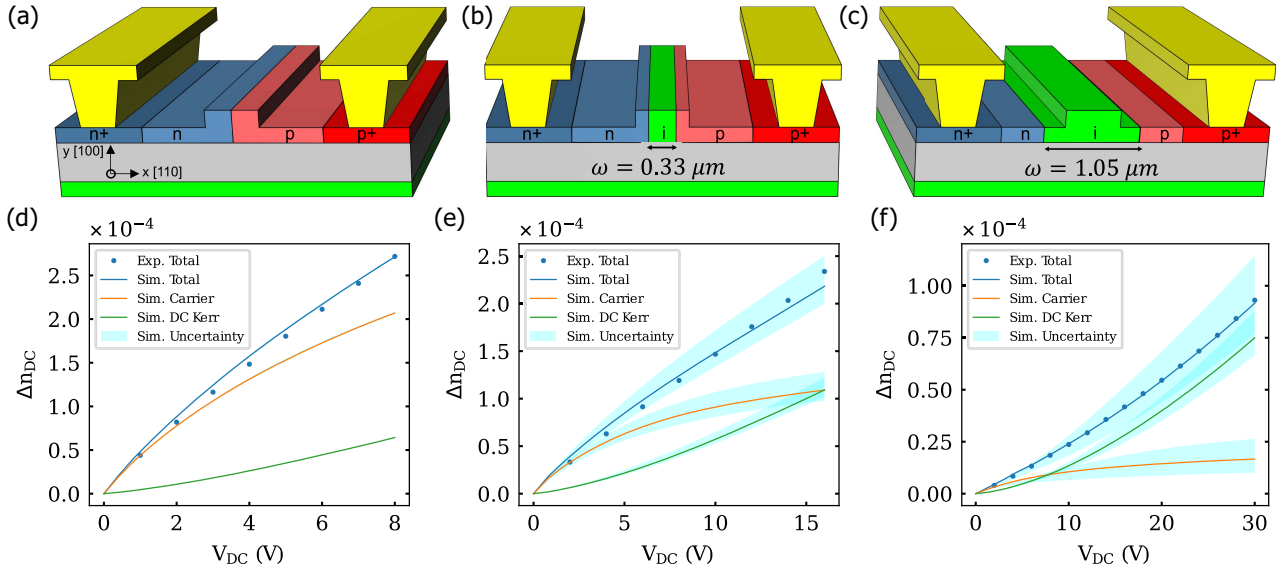

Fig. 1. (a) Depiction of PN junction, (b) PIN with intrinsic region width $w = 0.33\ \mu\mathrm{m}$ (PIN2), and (c) PIN with $w = 1.05\ \mu\mathrm{m}$ (PIN3). (d) Effective refractive index changes of PN, (e) PIN2, and (f) PIN3 junctions versus the applied reverse DC bias voltage with respective MZM arm lengths of 2, 6, and 6 mm. Dots are the experimental measurements, and lines correspond to the respective simulations of the whole modulation of the DC Kerr effect and carrier modulations.

Total refractive index modulations are in good agreement with the simulations. By increasing the width of the intrinsic region of the junction to 1.05 μm, the contribution of the plasma dispersion effect is significantly reduced to become minor compared to the DC Kerr effect, while it is dominant for the PN junction waveguide. The DC Kerr effect can, thus, contribute up to 82% of the total index change in the PIN3 junction waveguide.

B. Measurement of the EFI Linear EO Effect

The study of the EFI linear EO effect in the Ω angular frequency modulation focuses on the PIN3 junction, which shows a dominant contribution of the DC Kerr effect in the effective index change (4 times greater than the contribution from plasma dispersion) as seen in Fig. 1(f). A common DC bias voltage is applied to both arms of the MZM and a sinusoidal RF signal ($f = 5$ GHz) is split with two opposite phases to be applied in push–pull configuration. The optical wavelength is chosen to operate at the quadrature point. A simplified schematic view of the experimental setup to characterize the EOM is provided in Fig. 2(a). It is worthwhile to notice that the push–pull configuration of the MZM driving leads to assessing the index variation versus voltage as an equivalent efficiency of a single path because the measured index variation is twice the index variation in each arm while the considered voltage is twice of what is applied to each arm. The RF analysis in the push–pull configuration leads moreover to the cancellation of DC shift terms from Eq. (1) of the index variation in the MZM output measurements because the shift is the same in each arm.

The transfer function of the MZM as a function of the phase shift $\Delta\phi(t)$ is

$$\frac{P(t)}{P_0} = \frac{1}{2}\{1 + \cos[\Delta\phi(t) + \Delta\theta]\}, \tag{3}$$

with P_0 being the maximum output power of the MZM. The EOM response at the Ω angular frequency can be approximated at the quadrature point ($\Delta\theta = \pi/2$) as $P_\Omega(t) = P_0\Delta\phi(t)/2$ with $\Delta\phi(t) = m_\Omega \cos \Omega t$, m_Ω being the modulation index, $m_{\Omega,k}$ being the EFI linear EO modulation index, and $m_{\Omega,c}$ being the carrier modulation index,

$$m_\Omega = m_{\Omega,k} + m_{\Omega,c}, \tag{4}$$

$$m_{\Omega,k} = \Gamma\frac{2\pi}{\lambda}L_{\text{eff1}}\frac{3\chi^{(3)}}{n_{\text{si}}}F_{\text{DC}}F_{\text{RF}}, \tag{5}$$

with the mode overlap $\Gamma = 0.87$ in the Si waveguide, the effective length $L_{\text{eff1}} = [1 - \exp(-\alpha_{\text{RF}}L)]/\alpha_{\text{RF}}$, and the RF field loss $\alpha_{\text{RF}} = 4.3$ dB · cm^{-1}. See Appendices B and C for more details. Both the EFI linear EO effect and the plasma dispersion effect are expected to increase linearly with the RF amplitude. Only the EFI linear EO effect is expected to increase with the applied reverse DC bias following the Eq. (5). The dynamic carrier modulation is expected to decrease with V_{DC} considering a small signal approximation on its static response.

For a 6 mm long junction, a linear behavior of the effective index change $\Delta n_\Omega = m_\Omega\lambda/(2\pi L_{\text{eff1}})$ as a function of the applied reverse DC bias and RF amplitude is observed in Figs. 2(b) and 2(c), respectively. This is a clear signature of the EFI linear EO effect. In Fig. 2(b), the non-zero intersection and nonlinear behavior of Δn_Ω around $V_{\text{DC}} = 0$ V indicates that carrier modulation is dominant relative to the EFI linear EO effect at low reverse DC voltages. The slope of

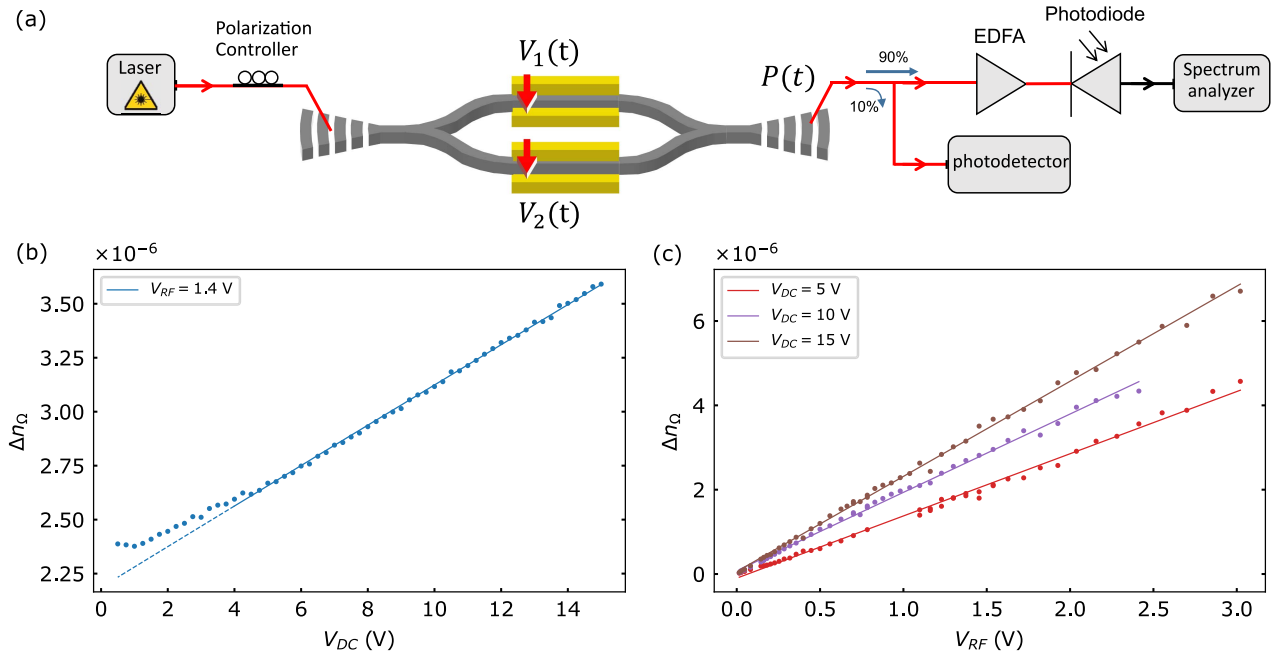

Fig. 2. (a) Schematic view of the experimental setup used to measure the EOM from the MZM. DC voltage is applied to both arms; RF is either applied in single-drive or push–pull configuration (EDFA, erbium-doped fiber amplifier). (b) Effective index variations measured in push–pull configuration versus the reverse DC bias for a fixed RF peak amplitude of 1.4 V, (c) versus the RF amplitude for three reverse DC biases.

the curve allows us to determine the $\chi^{(3)}$ coefficient ($\chi^{(3)} = 1.0 \times 10^{-19}$ m$^2 \cdot$ V^{-2}). See Appendices D and E for more information. This value is slightly underestimated (Appendix E) due to the carrier contribution having a negative evolution with V_{DC}. However, it remains relatively close to the $\chi^{(3)}$ values found in the literature.

C. Measurement of the Quadratic EO Effect

The quadratic EO effect at the angular frequency of 2Ω can only be observed in a single-drive configuration, as it is proportional to the square of the electric field. We studied the transfer function at angular frequencies of Ω and 2Ω to separate the modulation behavior resulting from the distortion produced by the nonlinear transfer function of the MZM [Eq. (3)] and the quadratic EO effect. A bandpass RF filter centered at Ω was placed at the signal generator output ensuring a very high rejection at 2Ω. We considered the PIN3 junction where distortion due to the carrier absorption modulation is negligible.

The phase shift induced by the plasma dispersion and the Kerr effects can then be written as

$$\Delta\phi(t) = m_\Omega \cos \Omega t + m_{2\Omega} \cos 2\Omega t, \tag{6}$$

where $m_{2\Omega}$ is the modulation index associated with the quadratic EO effect,

$$m_{2\Omega} = \Gamma \frac{2\pi}{\lambda} L_{\text{eff}2} \frac{3\chi^{(3)}}{4n_{\text{si}}} F_{\text{RF}}^2, \tag{7}$$

and $L_{\text{eff}2} = [1 - \exp(-2\alpha_{\text{RF}}L)]/(2\alpha_{\text{RF}})$ is the effective length for the 2Ω component.

The Ω and 2Ω components of the MZI spectral response can be written—after inserting the phase shift $\Delta\phi(t)$ [Eq. (6)] in the MZM transfer function $P(t)/P_0$ [Eq. (3)], performing a Jacobi–Anger expansion, and neglecting intermodulations—as follows:

$$\frac{P_\Omega(t)}{P_0} = \sin(\Delta\theta) J_1(m_\Omega) \cos \Omega t, \tag{8}$$

$$\frac{P_{2\Omega}(t)}{P_0} = [-\cos(\Delta\theta) J_2(m_\Omega) + \sin(\Delta\theta) J_0(m_\Omega) J_1(m_{2\Omega})] \cos 2\Omega t, \tag{9}$$

where $J_n(m_\Omega)$ represents the Bessel functions of the first kind.

The modulation indices m_Ω and $m_{2\Omega}$ are determined by fitting the DC transmission and the spectral responses using Eqs. (8) and (9) at fixed reverse DC and RF voltages. See Appendix F.

The measurements performed for a 5 mm long PIN3 junction [Fig. 3(a)] show that the 2Ω component is induced by the quadratic EO effect and not the signal distortion (the modulation operates at quadrature). Then, we can extract the corresponding modulation index $m_{2\Omega}$ from the response of the PIN3 junction. We can notice that it is, however, not possible to extract the $m_{2\Omega}$ modulation index from the responses of the PN and PIN2 junctions because the distortion induced by carriers is too important (see Appendix F, Fig. 7). The modulation indices m_Ω and $m_{2\Omega}$ are accurately extracted at different reverse DC and RF bias voltages for the PIN3 junction using this method.

Figure 3(b) shows the linear variation of the refractive index change $\Delta n_{2\Omega} = m_{2\Omega}\lambda/(2\pi L_{\text{eff}2})$ as a function of the square RF voltage (i.e., $\Delta n_{2\Omega}$ quadratically increases with the RF voltage). This variation is independent of the applied reverse DC voltage, as expected with a quadratic EO effect. In addition, a linear fit of $\Delta n_{2\Omega}$ with respect to F_{RF}^2 is performed to extract the $\chi^{(3)}$ coefficient ($\chi^{(3)} = 1.5 \times 10^{-19}$ m$^2 \cdot$ V^{-2}). This value is close to the average value from the literature and is consistent with the value found in the previous section.

Moreover, the measurements of the Ω and 2Ω components of the spectral response can be used to calculate the EFI linear EOM contribution to the modulation at Ω using Eqs. (5) and (7),

$$m_{\Omega,k} = 4 \frac{F_{\text{DC}} L_{\text{eff}1}}{F_{\text{RF}} L_{\text{eff}2}} m_{2\Omega}. \tag{10}$$

The DC electric field inside the PIN junction is estimated using $F_{\text{DC}} = (V_{\text{DC}} + V_{\text{bi}})/w$ with V_{bi} the built-in voltage

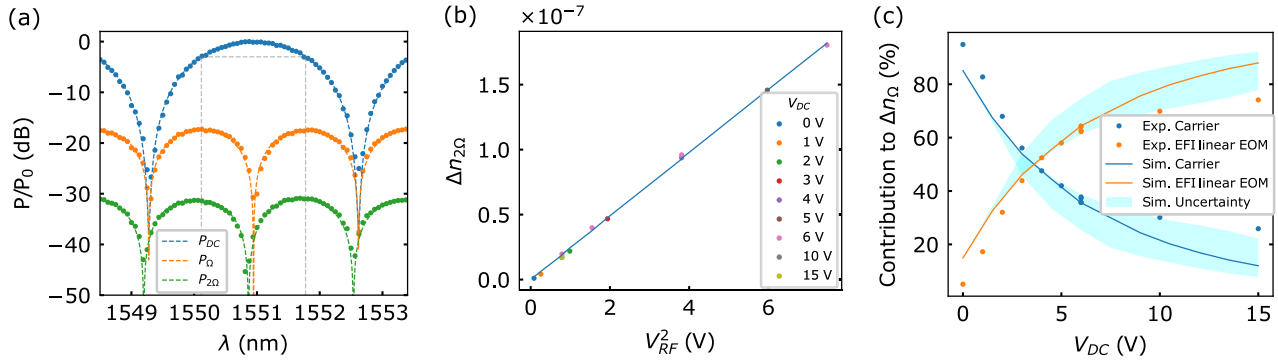

Fig. 3. Dots and the lines represent, respectively, the measurements and the corresponding fit or simulations. (a) Optical MZM transfer function for three electrical spectral components excluding intrinsic losses with P_0 the maximum output power, P_{DC} the static power, P_Ω the modulation power at angular frequency Ω, and $P_{2\Omega}$ at frequency 2Ω for the PIN3 junction by applying reverse $V_{\text{DC}} = 6$ V, $V_{\text{RF}} = 2.0$ V. (b) Amplitude of the refractive index modulation at angular frequency 2Ω versus the applied voltage V_{RF} at frequency Ω for reverse DC biases from 0 to 15 V. Whatever the value V_{DC}, it induces no variation of $\Delta n_{2\Omega}$. (c) Respective relative contribution of index variation in the Ω component from EFI linear EOM and from carrier modulation versus the applied reverse DC bias voltage.

and w the width of the intrinsic region [16]. See Appendix D. The RF field is estimated from the small signal approximation $F_{RF} \approx V_{RF} dF_{DC}/dV_{DC}$.

The contributions of the EFI linear EOM ($m_{\Omega,k}/m_{\Omega}$) and carrier modulation [$(m_{\Omega} - m_{\Omega,k})/m_{\Omega}$] in the Ω spectral response are reported in Fig. 3(c) showing that, above $V_{DC} = 5$ V and at a modulation frequency of 5 GHz, the EFI linear EO effect contribution to the modulation becomes greater than the carrier modulation and reaches more than a factor of 3 at 15 V. A good agreement with simulations from Fig. 1(f) is obtained.

D. Eye Diagram Experiments

The data transmission characteristics of EO modulators based on the DC Kerr effect using PIN3 diode have been analyzed. The DATA and $\overline{\text{DATA}}$ signals from an SHF bit pattern generator were amplified and transmitted to the respective arms of the MZM in push–pull configuration. A schematic view of the setup is shown in Fig. 4(a).

First, optical eye diagrams were acquired at 10 Gbit/s on a digital communication analyzer (DCA) from a 6 mm long modulator with each arm driven at $4V_{pp}$ and at different reverse DC bias voltages. The extinction ratio (ER) and the signal-to-noise ratio (SNR) of the modulated optical signal were computed by the DCA. The ER is greatly improved by reverse bias V_{DC} [Fig. 4(b)]. Indeed, for a V_{DC} varying from 2 to 30 V, the measured ER increases from 1.5 to 3.7 dB, and the SNR increases from 8.9 to 15.6. These results are entirely explainable with the EFI linear EO modulation behavior studied in Fig. 2. (More eye diagrams as a function of V_{DC} are presented in Appendix G, Fig. 8.)

At higher data rate, the DC Kerr effect improves the transmission capability, reaching a maximum data rate of 40 Gbit/s for the same 6 mm long PIN3 modulator with each arm driven at $4V_{pp}$ [Appendix G Fig. 9(b)]. Its speed is limited by the RF electrode bandwidth, which can be further improved by redesigning the traveling wave electrodes to achieve an expected EO bandwidth of about 40 GHz for 1 cm propagation length [21].

Then, the bandwidth limitation of DC Kerr modulators for higher speed optical modulation was investigated on shorter

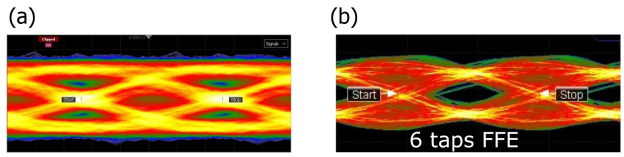

Fig. 5. Optical eye diagram display from 1 mm long PIN3 modulator by applying dual $2V_{pp}$ DATA/$\overline{\text{DATA}}$ driving in push–pull and reverse $V_{DC} = 30$ V measured at (a) 80 Gbit/s and (b) 100 Gbit/s with a numerical six taps feed-forward equalization (FFE).

modulators with 1 mm long PIN3 modulator with each arm driven at $2V_{pp}$. The obtained speed limit shows a closing of the eye diagram around 80 Gbit/s [Fig. 5(a)] imputed to the limited traveling wave electrodes bandwidth, which is the same as the achieved speed limit of 1 mm long conventional depletion modulation under same test setup [22]. At 100 Gbit/s, the use of numerical six taps feed-forward equalization (FFE) has led to the open eye diagram [Fig. 5(b)] showing that such a DC Kerr modulator associated with the proper equalizing equipment could be promising to achieve very high speed modulation.

E. Prospect

The speed of silicon DC Kerr modulators can be improved by designing better traveling wave electrode or by removing the substrate to increase the electrode bandwidth by reducing the high-frequency electrode losses and the mismatch between the optical and RF group indices [23]. The doping level in PIN junctions does not limit their high-frequency response as their intrinsic RC bandwidth is greater due to the reduced loaded capacitance. Additionally, simulation results show the PIN modulator leads to a low doping-induced insertion loss of 0.11 dB/mm to be compared to about 1.5 dB/mm [24] for normal PN junction waveguides with $V_{\pi}L$ 1.6 V · cm. The $V_{\pi}L$ for PIN phase shifter is estimated at 22 V · cm for the current device working at 10 Gbit/s with $26V_{DC}$–$30V_{DC}$. The low optical loss of PIN phase shifters at high reverse DC biases [25] allows to build high Q-factor silicon ring resonators based on the DC Kerr effect to improve frequency

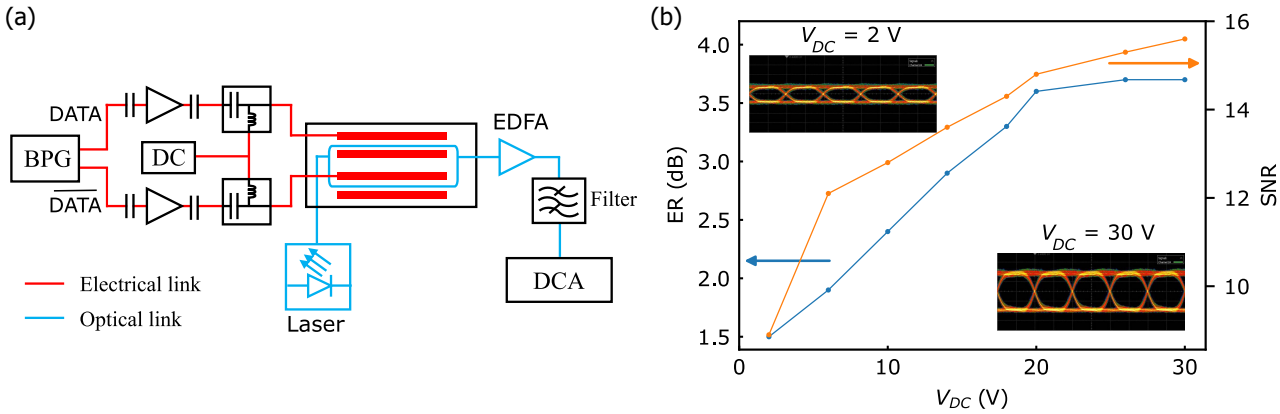

Fig. 4. (a) Setup used to acquire eye diagrams (PPG, pulse pattern generator; DC, reverse DC bias; EDFA, erbium-doped fiber amplifier; DCA, digital communications analyzer). (b) Extinction ratio and signal-to-noise ratio at 10 Gbit/s by applying dual $4V_{pp}$ DATA/$\overline{\text{DATA}}$ driving in push–pull versus the applied reverse DC bias. Eye diagrams for reverse DC bias of 2 and 30 V are embedded.

comb generation quality of ring modulators [26]. Such implementation of the DC Kerr ring modulator would reduce the footprint compared to MZI, and the speed limit will only be limited by the cavity quality factor. Because the maximum refractive index shift achievable using the DC Kerr effect is obtained when the electrical field inside the junction is maximum (close to the PIN junction avalanche) [27], a trade-off needs to be made among the high DC bias necessary to reach the maximum field, the carrier contribution, and the desired EO bandwidth limited by the RC constant, all increasing with the intrinsic region width [27]. Further improvements of the DC Kerr effect could be driven by optimizing the overlap between the optical and electric fields, i.e., the optical confinement in the waveguide and by carefully selecting the doping region to maximize the electric field location inside the waveguide.

3. CONCLUSION

The EFI Pockels effect (i.e., DC Kerr effect) has been observed in a Si PIN junction-based MZM. The refractive index variations as a function of both reverse DC bias voltage and RF amplitude have been measured in the dynamic regime showing a linear response with the DC bias voltage at a fixed RF amplitude. The refractive index modulations at angular frequencies Ω and 2Ω resulting from an applied RF signal at the angular frequency Ω have been extracted to quantify the EFI linear EO effect contribution to the modulation. We have shown that the DC Kerr effect is the main reason for the high-speed modulation above 5 V DC bias voltages in comparison with plasma dispersion effect. Furthermore, optical modulation has been demonstrated up to 100 Gbit/s for a 1 mm long MZM. Silicon modulators based on the EFI linear EO modulation show promising characteristics for high-speed optical communications when using in short MZMs or in ring modulators. But they can also be used in quantum and LIDAR applications, where the low loss and efficiency characteristics are more important than the high-speed one, using longer phase shifters thanks to the low loss of PIN junctions and pure phase modulation of Kerr effect.

APPENDIX A: STATIC MEASUREMENT

Figure 6 shows the optical transfer function of the Mach–Zehnder interferometer (MZI) exhibiting the resonance wavelength λ_r, the free spectral range FSR(λ_r), and the wavelength shift $\Delta\lambda_r$ at 0 and 30 V reverse DC biass.

APPENDIX B: EFFECTIVE INDEX AND CONFINEMENT FACTOR

The confinement factor of the TE mode needs to be considered to correctly estimate the experimental value of the $\chi^{(3)}$ coefficient.

Effective refractive index definition:

$$\Delta n_{\text{eff}} = \frac{2n_{\text{si}}}{N}\iint_{\text{wg}} |E|^2 \Delta n \mathrm{d}x\mathrm{d}y, \tag{B1}$$

with

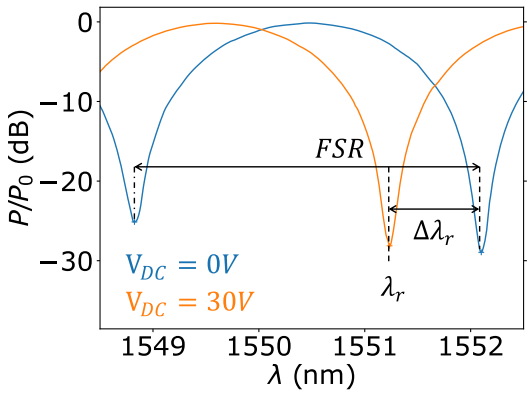

Fig. 6. Optical transmission of an unbalanced MZI for an applied reverse bias of 0 and 30 V. λ_r is the resonance wavelength, FSR(λ_r) the free spectral range, and $\Delta\lambda_r$ the wavelength shift for bias voltage variation from 0 to 30 V.

$$N = \frac{1}{c\epsilon_0}\iint_{\infty} (E \times H^* + E^* \times H)\cdot \hat{z}\mathrm{d}x\mathrm{d}y. \tag{B2}$$

The confinement factor can be generally defined as

$$\Gamma = \frac{2n_{\text{si}}}{N}\iint_{\text{wg}} |E|^2 \mathrm{d}x\mathrm{d}y, \tag{B3}$$

resulting in an effective refractive index,

$$\Delta n_{\text{eff}} = \Gamma \frac{\iint_{\text{wg}} |E|^2 \Delta n \mathrm{d}x\mathrm{d}y}{\iint_{\text{wg}} |E|^2 \mathrm{d}x\mathrm{d}y}. \tag{B4}$$

In the case of Kerr modulations, the refractive index becomes

$$\Delta n_{\text{eff}} = \Gamma \frac{3\chi^{(3)}}{2n_{\text{si}}} \frac{\iint_{\text{wg}} |E|^2 F^2(t) \mathrm{d}x\mathrm{d}y}{\iint_{\text{wg}} |E|^2 \mathrm{d}x\mathrm{d}y}. \tag{B5}$$

By assuming a constant $F(t)$ field inside the waveguide, the effective refractive index modulation becomes

$$\Delta n_{\text{eff}} = \Gamma \frac{3\chi^{(3)}}{2n_{\text{si}}} F^2(t). \tag{B6}$$

Therefore, the effective modulation of the Ω and 2Ω components of the spectral response can be written as

$$\Delta n_{\Omega} = \Gamma \frac{3\chi^{(3)}}{n_{\text{si}}} F_{\text{DC}} F_{\text{RF}} \cos \Omega t + \Delta n_{\text{carrier}}, \tag{B7}$$

$$\Delta n_{2\Omega} = \Gamma \frac{3\chi^{(3)}}{4n_{\text{si}}} F_{\text{RF}}^2 \cos 2\Omega t. \tag{B8}$$

APPENDIX C: EFFECTIVE LENGTH AND RF LOSSES

RF losses from our setup (RF filter, cables, splitter, a phase shifter, and RF probes) are measured to accurately estimate the values of the applied RF amplitude V_{RF} to the PIN junction. They are taken into account in V_{RF} for the corresponding output power P_{RF} displayed from the generator.

RF signal loss at the position z from the line is calculated using

$$F_{\mathrm{RF}}(z) = F_{\mathrm{RF}}(0)\exp(-\alpha_{\mathrm{RF}}z). \tag{C1}$$

The propagation losses of the RF line $\alpha_{\mathrm{RF}} = 4.3\ \mathrm{dB\cdot cm^{-1}} = 50\ \mathrm{m^{-1}}$ were extracted from RF transmissions at different line length. These losses need to be taken into account in the phase shift equation to define the effective lengths.

Phase variation equation:

$$\Delta\phi = \frac{2\pi}{\lambda}\int_0^L \Delta n \mathrm{d}z. \tag{C2}$$

The modulation index of the electric field-induced (EFI) linear electro-optic (EO) effect at the Ω spectral component is calculated using Eqs. (B7) and (C2),

$$m_{\Omega,k} = \Gamma\frac{2\pi}{\lambda}\int_0^L \frac{3\chi^{(3)}}{n_{\mathrm{si}}}F_{\mathrm{DC}}F_{\mathrm{RF}}\ \exp(-\alpha z)\mathrm{d}z, \tag{C3}$$

$$m_{\Omega,k} = \Gamma\frac{2\pi}{\lambda}L_{\mathrm{eff}1}\frac{3\chi^{(3)}}{n_{\mathrm{si}}}F_{\mathrm{DC}}F_{\mathrm{RF}}. \tag{C4}$$

The effective length for this Ω component is defined as

$$L_{\mathrm{eff}1} = \frac{1-\exp(-\alpha_{\mathrm{RF}}L)}{\alpha_{\mathrm{RF}}}. \tag{C5}$$

The modulation index of the quadratic EO effect at the 2Ω component is calculated using Eqs. (B8) and (C2),

$$m_{2\Omega} = \Gamma\frac{2\pi}{\lambda}\int_0^L \frac{3\chi^{(3)}}{4n_{\mathrm{si}}}F_{\mathrm{RF}}^2\ \exp(-2\alpha z)\mathrm{d}z, \tag{C6}$$

$$m_{2\Omega} = \Gamma\frac{2\pi}{\lambda}L_{\mathrm{eff}2}\frac{3\chi^{(3)}}{4n_{\mathrm{si}}}F_{\mathrm{RF}}^2. \tag{C7}$$

The effective length for this 2Ω component is defined as

$$L_{\mathrm{eff}2} = \frac{1-\exp(-2\alpha_{\mathrm{RF}}L)}{2\alpha_{\mathrm{RF}}}. \tag{C8}$$

APPENDIX D: FIELD INSIDE THE JUNCTION

The DC electric field inside the PIN junction is estimated to be

$$F_{\mathrm{DC}} = \frac{V_{\mathrm{DC}}+V_{\mathrm{bi}}}{w}, \tag{D1}$$

with the built-in voltage V_{bi} being

$$V_{\mathrm{bi}} = \frac{kT}{q}\ln\left(\frac{N_A N_D}{n_i^2}\right) \tag{D2}$$

and the intrinsic region w being

$$w = w_i + \sqrt{\frac{2\epsilon_0\epsilon_{\mathrm{Si}}}{q}\cdot\frac{N_A+N_D}{N_A N_D}}\sqrt{V_{\mathrm{bi}}+V_{\mathrm{DC}}}. \tag{D3}$$

For the PIN3 junction, the doping levels of boron (N_A) in the P region and of phosphorus (N_D) in the N region are $N_A = N_D = 10^{20}\ \mathrm{cm^{-3}}$. The intrinsic region has a Boron doping level of $n_i = 10^{15}\ \mathrm{cm^{-3}}$. $\epsilon_{\mathrm{Si}} = 11.9$ is the relative permittivity of silicon, resulting in $V_{\mathrm{bi}} = 0.6$ V and $w = 1050 + 5\sqrt{V_{\mathrm{DC}}+0.6}$ nm.

The RF field is estimated from the small signal approximation,

$$F_{\mathrm{RF}} \approx \frac{\mathrm{d}F_{\mathrm{DC}}}{\mathrm{d}V_{\mathrm{DC}}}V_{\mathrm{RF}}. \tag{D4}$$

Note that this approximation is particularly relevant for the PIN3 junction, even for high RF voltages, due to the small variation of the intrinsic width with the applied reverse DC bias ($\mathrm{d}F_{\mathrm{DC}}/\mathrm{d}V_{\mathrm{DC}} \approx 1/w_i$).

APPENDIX E: DETERMINATION OF THE EFI LINEAR EO EFFECT

In the push–pull experiment, the amplitude of the EFI linear EO modulation (at Ω component) is estimated from the slope of the DC sweep using Eq. (B7),

$$\frac{\mathrm{d}\Delta n_\Omega}{\mathrm{d}F_{\mathrm{DC}}} = \Gamma\frac{3\chi^{(3)}}{n_{\mathrm{si}}}F_{\mathrm{RF}} + \Gamma\frac{3\chi^{(3)}}{n_{\mathrm{si}}}F_{\mathrm{DC}}\frac{\mathrm{d}F_{\mathrm{RF}}}{\mathrm{d}F_{\mathrm{DC}}} + \frac{\mathrm{d}\Delta n_{\mathrm{carrier}}}{\mathrm{d}F_{\mathrm{DC}}}. \tag{E1}$$

For the PIN3 junction, the RF field variation with the DC field is small due to the small intrinsic region width variation with the applied DC bias and can be neglected ($\mathrm{d}F_{\mathrm{RF}}/\mathrm{d}F_{\mathrm{DC}} \propto \mathrm{d}^2F_{\mathrm{DC}}/\mathrm{d}V_{\mathrm{DC}}^2 \approx 0$). The carrier variation is, however, not neglectable and is expected to be negative ($\mathrm{d}\Delta n_{\mathrm{carrier}}/\mathrm{d}F_{\mathrm{DC}} < 0$), resulting in an underestimation of the $\chi^{(3)}$ coefficient using the slope of the measurement:

$$\chi^{(3)} \geq \frac{\mathrm{d}\Delta n_\Omega}{\mathrm{d}F_{\mathrm{DC}}}\frac{n_{\mathrm{si}}}{3\Gamma F_{\mathrm{RF}}}. \tag{E2}$$

APPENDIX F: FITTING THE SPECTRAL COMPONENTS

The output DC optical power P_{DC} of the MZI and the Ω and 2Ω components of the spectral response are measured as a function of the wavelength for a fixed DC bias and RF modulation. Their respective noise is subtracted.

The expected components are

$$\frac{P_{\mathrm{DC}}}{P_0} = \frac{1}{2}[1+\cos(\Delta\theta)J_0(m_\Omega)J_0(m_{2\Omega})], \tag{F1}$$

$$\frac{P_\Omega(t)}{P_0} = [-\cos(\Delta\theta)J_1(m_\Omega)J_1(m_{2\Omega}) + \sin(\Delta\theta)J_0(m_{2\Omega})J_1(m_\Omega)]\cos\ \Omega t, \tag{F2}$$

$$\frac{P_{2\Omega}(t)}{P_0} = \{-\cos(\Delta\theta)[J_0(m_{2\Omega})J_2(m_\Omega) - J_2(m_\Omega)J_2(m_{2\Omega})] + \sin(\Delta\theta)J_0(m_\Omega)J_1(m_{2\Omega})\}\cos\ 2\Omega t. \tag{F3}$$

In the main paper, these equations are approximated assuming a small modulation index $m_{2\Omega}$ resulting in $J_0(m_{2\Omega}) \approx 1$, $J_1(m_\Omega)J_1(m_{2\Omega})$, and $J_2(m_{2\Omega}) \approx 0$.

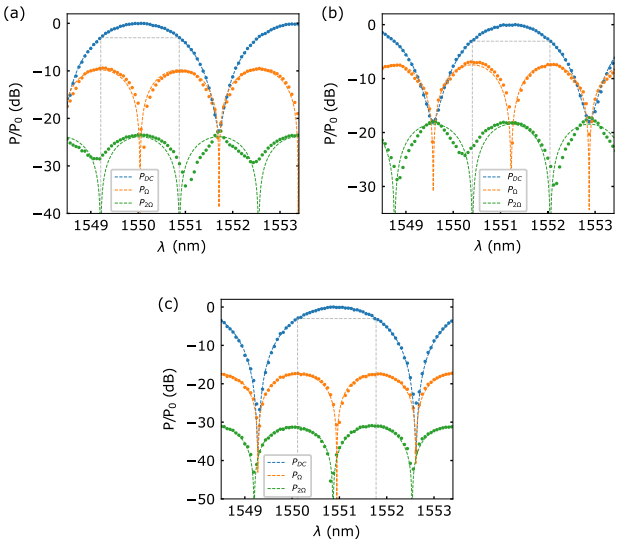

Fig. 7. Measurements (dots) of P_{DC}, the MZM output DC optical power; P_{Ω}, the modulation at angular frequency Ω; $P_{2\Omega}$, the modulation at angular frequency 2Ω as a function of wavelength for (a) the 2 mm long PN junction using $V_{DC} = 2$ V, $V_{RF} = 0.51$ V, (b) the 5 mm long PIN2 junction using $V_{DC} = 4$ V, $V_{RF} = 1.6$ V, and (c) the 5 mm long PIN3 junction using $V_{DC} = 6$ V, $V_{RF} = 2.0$ V. The dashed lines represent the corresponding fit.

First, we fit the static phase variation $\Delta\theta$ of the DC curve using Eq. (F1) to extract the period of the MZM assuming no dynamic modulation. This value is then used in Eq. (F2) to fit the modulation m_{Ω} index at the Ω spectral component assuming $m_{2\Omega} = 0$. Then we find the modulation $m_{2\Omega}$ at the 2Ω spectral component by fitting Eq. (F3) using the previously found parameters as initial guess.

Figure 7 shows one of the measurements done for each of the three studied junctions. Only the PIN3 junction [Fig. 7(c)] has a 2Ω component with a modulation higher than the MZM distortion, resulting in a 2Ω component aligned with the Ω component. For the two other junctions [Figs. 7(a) and 7(b)], the 2Ω component comes from the distortion, and the $m_{2\Omega}$ coefficient cannot be extracted. Moreover, their spectral components do not fit as well with Eq. (F3) as for the PIN3 junction. One possible reason could be that, for those modulators, the carrier absorption introduces a chirp effect that has not been taken into account in the analyses.

APPENDIX G: EYE DIAGRAM EXPERIMENTS

Figure 8 shows some of the eye diagrams used to plot the evolution of the ER and SNR with V_{DC} in the main article, respectively, measured at 2, 10, 18, and 30 V reverse bias for a 10 Gbit/s modulation by applying dual $4V_{pp}$ DATA/$\overline{\text{DATA}}$ driving in push–pull. The displays use the averaging function of the DCA to reduce optical noise from EDFA.

Figure 9(a) shows a data rate transfer of 32 Gbit/s, and Fig. 9(b) shows a maximum data rate transfer of 40 Gbit/s achieved with the 6 mm long PIN3 based MZI.

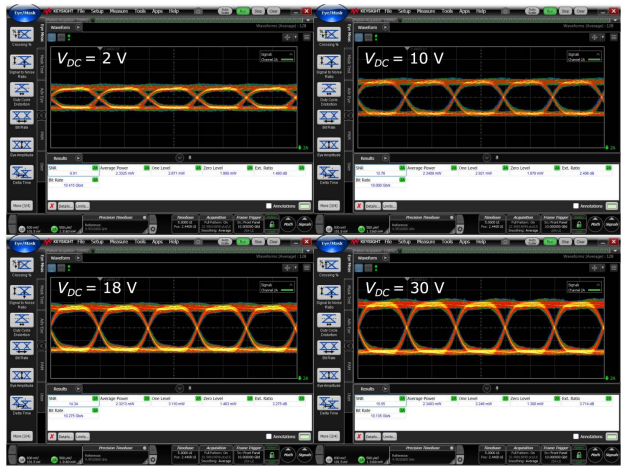

Fig. 8. Eye diagram, respectively, measured at 2, 10, 18, 30 V reverse DC bias at 10 Gbits/s using $4V_{pp}$ on each arm corresponding to ER 1.5, 2.4, 3.3, and 3.7 dB, and SNR 8.9, 12.8, 14.3, 15.6 dB.

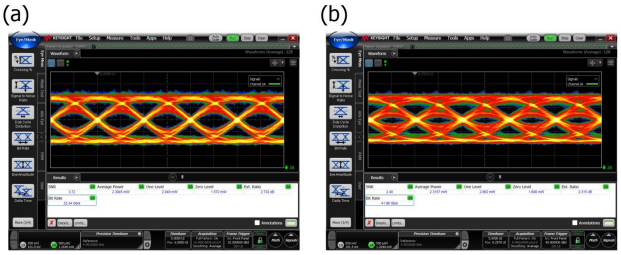

Fig. 9. Optical eye diagram of 6 mm long PIN3 modulator measured at a data rate of (a) 32 Gbit/s and (b) 40 Gbit/s using $4V_{pp}$ on each arm and reverse $V_{DC} = 30$ V, with ER 2.7 dB and 2.3 dB, respectively.

APPENDIX H: SAMPLE FABRICATION

The silicon MZI modulators are fabricated through silicon photonics foundry CORNERSTONE [28], which provides detailed fabrication steps based on 8-inch 220 nm SOI wafers and doping information. The passive waveguides were etched with 250 nm thickness patterned PECVD oxide hard mask. The hard mask also protects the silicon core during the n-type implantation process. The junction is optimized through the

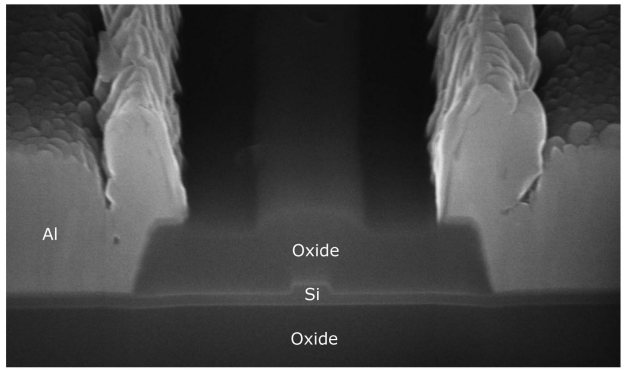

Fig. 10. Cross section of the fabricated device viewed with an SEM.

self-aligned doping steps in Ref. [28] for the studied PN and PIN junctions. Figure 10 shows an SEM image of the cross section of the fabricated device.

APPENDIX I: SETUP FOR DYNAMIC MEASUREMENTS

A T100S-HP tunable laser is used to inject light into the device via the grating couplers. A polarization controller is used to ensure a TE-mode injection. A 90/10 splitter is used to separate the output power; 10% goes into a CT400 optical components tester to measure the DC optical power, and 90% goes to a Keopsys KPS prebooster set to output a constant 3 dBm power. The amplified modulated optical signal is collected using a Agilent 83440D photodiode and fed to an Anritsu MS2830A signal analyzer set to monitor either the Ω or 2Ω components of the spectral response. A Keithley 2401 is used for polarized PIN junctions. The RF signals are generated using an Anritsu MG3694C signal generator. The signal is then coupled with the DC bias voltage using a Anritsu V251 bias-T. For push–pull experiments, the RF signal is split in half using an Anritsu V241C power splitter, and a phase delay is introduced on one arm using a Waka 02X0518-00 phase shifter. ACP 50 GHz GSGSG RF probes are used to apply the DC and RF bias voltages to the traveling wave electrodes. Measurements are done at the quadrature point by tuning the laser wavelength.

APPENDIX J: SETUP FOR EYE DIAGRAM MEASUREMENTS

MZI modulators are differentially driven with combined V_{RF} and V_{DC} by using two high-voltage bias tees (SHF BT45R – HV100). The high-speed signals are generated from an SHF bit pattern generator and amplified to $4V_{pp}$ on each arm for modulation rates below 50 Gbit/s and to $2V_{pp}$ for higher modulation rates up to 100 Gbit/s. NRZ signals are sent to the MZI modulators via 67 GHz GSGSG probes and terminated with DC blocks and 50 mΩ resistors. Measurements are done at the quadrature point. Eye diagrams are displayed using the averaging function of the DCA to reduce optical noise from EDFA.

Funding. Engineering and Physical Sciences Research Council (EP/N013247/1, EP/T019697/1); Royal Society (UF150325).

Acknowledgment. The authors acknowledge CORNERSTONE team of University of Southampton for the device fabrication. J. Peltier acknowledge Victor Turpaud for fruitful discussions, and Quentin Chateiller and Bruno Garbin for the development of the Python package Autolab used in his experiments. D. J. Thomson acknowledges funding from the Royal Society for his University Research Fellowship.

Disclosures. The authors declare no conflicts of interest.

Data Availability. Data underlying the results presented in this paper are available from the corresponding authors upon reasonable request.

REFERENCES

1. A. Rahim, A. Hermans, and B. Wohlfeil, *et al.*, "Taking silicon photonics modulators to a higher performance level: state-of-the-art and a review of new technologies," Adv. Photonics **3**, 024003 (2021).
2. G. Sinatkas, T. Christopoulos, and O. Tsilipakos, *et al.*, "Electro-optic modulation in integrated photonics," J. Appl. Phys. **130**, 010901 (2021).
3. M. Berciano, G. Marcaud, and P. Damas, *et al.*, "Fast linear electro-optic effect in a centrosymmetric semiconductor," Commun. Phys. **1**, 64 (2018).
4. M. He, M. Xu, and Y. Ren, *et al.*, "High-performance hybrid silicon and lithium niobate Mach–Zehnder modulators for 100 Gbit s^{-1} and beyond," Nat. Photonics **13**, 359–364 (2019).
5. A. C. Liu, M. J. F. Digonnet, and G. S. Kino, "Measurement of the dc Kerr and electrostrictive phase modulation in silica," J. Opt. Soc. Am. B **18**, 187–194 (2001).
6. Z. Chen, J. Zhao, and Y. Zhang, *et al.*, "Pockel's effect and optical rectification in (111)-cut near-intrinsic silicon crystals," Appl. Phys. Lett. **92**, 251111 (2008).
7. J.-C. Zhu, Z.-G. Chen, and X.-H. Liu, *et al.*, "Investigation on the electric-field-induced Pockels effect and optical rectification in near-intrinsic silicon samples," Opt. Laser Technol. **44**, 582–586 (2012).
8. S. B. Bodrov, Y. A. Sergeev, and A. I. Korytin, *et al.*, "Terahertz-field-induced second optical harmonic generation from Si(111) surface," Phys. Rev. B **105**, 035306 (2022).
9. O. V. Chefonov, A. V. Ovchinnikov, and M. B. Agranat, "Study of second optical harmonic generation in terahertz pulse-induced antiferromagnetic NiO," Quantum Electron. **52**, 269 (2022).
10. P. Steglich, C. Villringer, and B. Dietzel, *et al.*, "Electric field-induced linear electro-optic effect observed in silicon-organic hybrid ring resonator," IEEE Photonics Technol. Lett. **32**, 526–529 (2020).
11. A. Friedman, H. Nejadriahi, and R. Sharma, *et al.*, "Demonstration of the DC-Kerr effect in silicon-rich nitride," Opt. Lett. **46**, 4236–4239 (2021).
12. L.-Y. S. Chang, H. Nejadriahi, and S. Pappert, *et al.*, "Demonstration of DC Kerr effect induced high nonlinear susceptibility in silicon rich amorphous silicon carbide," Appl. Phys. Lett. **120**, 071107 (2022).
13. B. Zabelich, E. Nitiss, and A. Stroganov, *et al.*, "Linear electro-optic effect in silicon nitride waveguides enabled by electric-field poling," ACS Photonics **9**, 3374–3383 (2022).
14. E. Timurdogan, C. V. Poulton, and M. J. Byrd, *et al.*, "Electric field-induced second-order nonlinear optical effects in silicon waveguides," Nat. Photonics **11**, 200–206 (2017).
15. C. G. Bottenfield, V. A. Thomas, and S. E. Ralph, "Silicon photonic modulator linearity and optimization for microwave photonic links," IEEE J. Sel. Top. Quantum Electron. **25**, 3400110 (2019).
16. A. Jain, N. Hosseinzadeh, and X. Wu, *et al.*, "A high spur-free dynamic range silicon dc Kerr ring modulator for RF applications," J. Lightwave Technol. **37**, 3261–3272 (2019).
17. P. Xia, H. Yu, and H. Yu, *et al.*, "High linearity silicon DC Kerr modulator enhanced by slow light for 112 Gbit/s PAM4 over 2 km single mode fiber transmission," Opt. Express **30**, 16996–17007 (2022).
18. U. Chakraborty, U. Chakraborty, and J. Carolan, *et al.*, "Cryogenic operation of silicon photonic modulators based on the DC Kerr effect," Optica **7**, 1385–1390 (2020).
19. N. K. Hon, R. Soref, and B. Jalali, "The third-order nonlinear optical coefficients of Si, Ge, and $Si_{1-x}Ge_x$ in the midwave and longwave infrared," J. Appl. Phys. **110**, 011301 (2011).
20. J. Zhang, Q. Lin, and G. Piredda, *et al.*, "Anisotropic nonlinear response of silicon in the near-infrared region," Appl. Phys. Lett. **91**, 071113 (2007).
21. Y. Yang, Q. Fang, and M. Yu, *et al.*, "High-efficiency Si optical modulator using Cu travelling-wave electrode," Opt. Express **22**, 29978–29985 (2014).
22. K. Li, D. Thomson, and S. Liu, *et al.*, "112G baud sub pJ/bit integrated CMOS-silicon photonics transmitter," Research Square, PPR540568 (2022).

23. M. Li, L. Wang, and X. Li, *et al.*, "Silicon intensity Mach–Zehnder modulator for single lane 100 Gb/s applications," Photonics Res. **6**, 109–116 (2018).
24. J. X. B. Sia, X. Li, and J. Wang, *et al.*, "Wafer-scale demonstration of low-loss (≈0.43 dB/cm), high-bandwidth (>38 GHz), silicon photonics platform operating at the C-band," IEEE Photonics J. **14**, 6628609 (2022).
25. H. Rong, A. Liu, and R. Jones, *et al.*, "An all-silicon Raman laser," Nature **433**, 292–294 (2005).
26. M. Zhang, B. Buscaino, and C. Wang, *et al.*, "Broadband electro-optic frequency comb generation in a lithium niobate microring resonator," Nature **568**, 373–377 (2019).
27. C. G. Bottenfield, V. A. Thomas, and S. E. Ralph, "DC Kerr effect and limits for silicon photonic modulators," in *Conference on Lasers and Electro-Optics (CLEO)* (2019), paper JTh2A.65.
28. C. G. Littlejohns, D. J. Rowe, and H. Du, *et al.*, "CORNERSTONE's silicon photonics rapid prototyping platforms: current status and future outlook," Appl. Sci. **10**, 8201 (2020).